Electronic Supplemental Information for:

4f-Orbital Mixing Increases the Magnetic Susceptibility of Cp'$_3$Eu†

S. Olivia Gunther,[a‡] Yusen Qiao,[a‡] Patrick W. Smith,[a] Sierra R. Ciccone,[b] Alexander S. Ditter,[a] Daniel N. Huh,[b¶] Liane M. Moreau,[a,c] David K. Shuh,[a] Taoxiang Sun,[d] Polly L. Arnold,[a,e] Corwin H. Booth,[a] Wibe A. de Jong,[f] William J. Evans,[b] Wayne W. Lukens, Jr.,[a] Stefan G. Minasian[a]

[a] *Chemical Sciences Division, Lawrence Berkeley National Laboratory, Berkeley, CA 94720, USA.*

[b] *Department of Chemistry, University of California, Irvine, CA 92697, USA*

[c] *Department of Chemistry, Washington State University, Pullman, WA 99164, USA*

[d] *Institute of Nuclear and New Energy Technology, Tsinghua University, Beijing 100084, P.R. China*

[e] *Department of Chemistry, University of California, Berkeley, CA 94720, USA*

[f] *Computational Research Division, Lawrence Berkeley National Laboratory, Berkeley, CA 94720*

Table of Contents:

General Considerations. Unless specified otherwise, manipulations for the synthesis of organometallic complexes and the preparation of spectroscopic samples were performed under an Ar atmosphere using standard Schlenk line and glovebox techniques. Organic solvents were deoxygenated (by purging) and dried using an MBraun SPS 7 Solvent Purification System and stored over molecular sieves in an Ar-filled glove box. Samples of Cp'_3Eu and Cp'_3Gd were synthesized according to previously reported procedures.[1, 2]

Modified synthesis of Cp'_3Yb. KCp′ (68 mg, 0.38 mmol, 3.1 eq) was dissolved in THF and added to a suspension of YbI_3•$(THF)_{3.5}$ (100 mg, 0.12 mmol, 1 eq). The reaction was heated in a glovebox at 40 °C overnight. After about 16 hours, the reaction appeared as a red solution with a few dark green solids. The THF was removed under reduced pressure and the red/green residue was taken up in hexanes. The reaction continued to heat at 40 °C for another 16 hours affording a deep green solution with colorless solids. The reaction mixture was filtered through a plug of Celite to remove residual KI and the solvent was stripped away from the desired complex to afford a dark green microcrystalline solid. The solids were dissolved in the minimum amount of pentane and placed in a -35 °C glovebox freezer to afford green needles of Cp'_3Yb (57 mg, 78% yield). The ^{1}H NMR spectrum was consistent with what has been previously reported in the literature.[2]

Magnetic Measurements. Magnetic data for Cp'_3Eu was modeled by fitting the data in Excel for the atomic and configuration interaction models and using the program CONDON 3.0[3] for the crystal field model. In all cases, the quantity minimized was $\sum_i \frac{(\chi_{data}-\chi_{calc})^2}{\chi^2_{data}}$. The atomic model (free-ion model) is described in the text. The crystal field model (CONDON 3.0) requires starting values for spin-orbit coupling, electron-electron repulsion (Slater parameters), and crystal field parameters. These values are known for Cp'_3Nd; however, no similar system has been studied for Eu.[4]

The parameters needed to model the susceptibility of Cp'_3Eu assuming C_{3h} symmetry are the spin-orbit coupling constant, ζ (ζ is equal to 2**S**λ), three Slater electron repulsion parameters, F^2, F^4, and F^6, and four crystal field parameters B_0^2, B_0^4, B_0^6, and B_6^6. The parameters that have the greatest impact on the magnetic susceptibility are the crystal field parameters (B_0^2, B_0^4, B_0^6, and B_6^6), ζ , and the Stevens orbital reduction factor, k. ζ and k are strongly correlated, so either one or the other is varied (allowing both to vary may not improve the model as is the case here). To fit the data, starting values are needed for all of the parameters. Few sets of parameters are available for Eu(III), but many sets of parameters are available for Nd(III), including those for Cp'_3Nd.[4] In addition, parameters for both $Eu(H_2O)_9(ES)_3$ and $Nd(H_2O)_9(ES)_3$, where ES is ethylsulfate, are available.[5] Since $Eu(H_2O)_9(ES)_3$ has D_{3h} symmetry, which uses the same set of parameters as C_{3h} symmetry, starting parameters for Cp'_3Eu were obtained by multiplying the parameters for Cp'_3Nd by ratio of the $Eu(H_2O)_9(ES)_3$ parameters to those of $Nd(H_2O)_9(ES)_3$. These values are given in

Table S1. The data was initially modeled by leaving ζ fixed at 1336 cm^{-1} and fitting the magnetic susceptibility with k=0.99999 through 0.45 in steps of 0.05. Once the fit had converged, ζ was changed by 100 cm^{-1} and allowed to vary. In all cases, the fits with ζ fixed at 1336 cm^{-1} had smaller reduced χ^2 (χ_v^2), so only the fits with fixed ζ were examined further. The results of all fits are given in Tables S2 through S5. Fits for k=0.95 (best fit), 0.7 (k most similar to n_f from XAS measurements and with reasonable fit parameters), and 0.55 (best fit with reasonable crystal field parameters) are given in Figures S1-S3 (they look almost identical to each other).

Table S1. Starting crystal field parameters associated with fitting the magnetic susceptibility of Cp'_3Eu

Parameter	Starting values
k [a]	1
ζ (cm^{-1})	1336
F^2 (cm^{-1})	79651
F^4 (cm^{-1})	60067
F^6 (cm^{-1})	44020
B_0^2 (cm^{-1})	-2149
B_0^4 (cm^{-1})	941
B_0^6 (cm^{-1})	756
B_6^6 (cm^{-1})	-2195

Table S2. "high" crystal field parameters determined by fitting the magnetic susceptibility of Cp'$_3$Eu (these parameters are too large to be correct but best fit the data). Energies in cm^{-1}.

k	B^2_0	B^4_0	B^6_0	B^6_6	ζ^a	χ^2	χ_v^2	$w\chi^{2b}$
1.00	-50862	-27972	-53867	-10281	1336	0.0073	0.0024	5.0
0.95[c]	-74367	-23727	-45062	-9107	1336	0.0044	0.0015	3.0
0.90	-75272	-23516	-43308	-8460	1336	0.0044	0.0015	3.0
0.85	-76131	-23392	-41335	-7793	1336	0.0045	0.0015	3.1
0.80	-77103	-23338	-38884	-7099	1336	0.0046	0.0015	3.2
0.75	-78324	-23348	-35659	-6370	1336	0.0047	0.0016	3.2
0.70	-80247	-23461	-30574	-5587	1336	0.0047	0.0016	3.2
0.65	-82388	-21418	-26189	-4805	1334	0.0047	0.0016	3.2
0.60	-85125	-16296	-21823	-3960	1336	0.0046	0.0015	3.2
0.55	-88063	-9094	-17401	-2909	1336	0.0049	0.0016	3.3
0.50	-90128	-2730	-14274	-1473	1336	0.0058	0.0019	4.0
0.45	-90100	-2571	-14206	-1	1336	0.0280	0.0093	19.2

a) ζ fixed at 1336 cm^{-1}
b) χ^2 weights so that the best fit has χ^2= DOF
c) Best fit

Table S3. "high" crystal field parameters while varying ζ determined by fitting the magnetic susceptibility of Cp'$_3$Eu (based on χ_v^2, these parameters fit the data less well than those in Table S2). Energies in cm^{-1}.

k	B^2_0	B^4_0	B^6_0	B^6_6	ζ	χ^2	χ_v^2	$w\chi^{2a}$
1.00[b]	-66176	-25120	-56894	-8458	1139	0.0042	0.0021	2.0
0.95	-74190	-23693	-45524	-9024	1324	0.0044	0.0022	2.1
0.90	-75215	-23502	-43473	-8425	1331	0.0044	0.0022	2.1
0.85	-76222	-23398	-41157	-7789	1336	0.0045	0.0023	2.1
0.80	-77289	-23364	-38465	-7111	1340	0.0046	0.0023	2.2
0.75	-78629	-23404	-34937	-6390	1342	0.0047	0.0024	2.2
0.70	-80374	-23491	-30260	-5601	1339	0.0047	0.0024	2.2
0.65	-82405	-21382	-26162	-4772	1330	0.0046	0.0023	2.2
0.60	-85142	-16281	-21809	-3990	1342	0.0046	0.0023	2.2
0.55	-88069	-9090	-17397	-2925	1339	0.0048	0.0024	2.3
0.50	-8702	10772	-17079	-2248	1217	0.0049	0.0024	2.3
0.45	-90093	-2529	-14188	2	1387	0.0240	0.0120	11.3

a) χ^2 weights so that the best fit has χ^2= DOF
b) Best fit

Table S4. "Low" crystal field parameters determined by fitting the magnetic susceptibility of Cp'_3Eu (these parameters have reasonable values for $0.45 < k < 0.8$). Energies in cm^{-1}.

k	B^2_0	B^4_0	B^6_0	B^6_6	ζ^a	χ^2	χ_v^2	$w\chi^{2b}$
1.00	-50737	-28193	-53763	-10271	1336	0.0073	0.0024	4.3
0.95	-22362	10594	52761	-9455	1336	0.0073	0.0024	4.3
0.90	-21830	5496	51077	-8766	1336	0.0071	0.0024	4.3
0.85	-20736	-2123	47264	-8164	1336	0.0069	0.0023	4.1
0.80	-20227	-7224	43191	-7781	1336	0.0065	0.0022	3.9
0.75	-2498	1619	2294	-6722	1336	0.0082	0.0027	4.9
0.70	-2710	2349	1917	-5970	1336	0.0066	0.0022	4.0
0.65	-3529	504	1679	-5378	1336	0.0056	0.0019	3.3
0.60	-5478	-4527	-3378	-4887	1336	0.0052	0.0017	3.1
0.55[c]	-7532	-8274	-5328	-4241	1336	0.0050	0.0017	3.0
0.50	-9130	-10415	-5072	-3350	1336	0.0051	0.0017	3.0
0.45	-10603	-11933	-4216	-2009	1336	0.0052	0.0017	3.1

a) ζ fixed at 1336 cm^{-1}

b) χ^2 weights so that the best fit has χ^2= DOF

c) Best fit

Table S5. "Low" crystal field parameters while varying ζ determined by fitting the magnetic susceptibility of Cp'_3Eu (these parameters have reasonable values for $0.45 < k < 0.6$). Energies in cm^{-1}.

k	B^2_0	B^4_0	B^6_0	B^6_6	ζ	χ^2	χ_v^2	$w\chi^{2a}$
1.00	-66165	-25125	-56898	-8458	1139	0.0042	0.0021	1.7
0.95	-22903	12466	54088	-9318	1312	0.0073	0.0036	3.0
0.90	-17394	-23070	3580	-12926	1598	0.0053	0.0026	2.2
0.85	-17071	-22379	3045	-11999	1584	0.0053	0.0026	2.2
0.80	-16199	-20992	2503	-11010	1567	0.0052	0.0026	2.1
0.75	-16828	-21610	1137	-10066	1553	0.0052	0.0026	2.1
0.70	-14682	-18822	-521	-8869	1523	0.0052	0.0026	2.1
0.65	-11911	-15173	-2966	-7424	1474	0.0052	0.0026	2.1
0.60	-8735	-10447	-4905	-5688	1398	0.0051	0.0026	2.1
0.55	-7315	-8254	-8993	-3938	1307	0.0050	0.0025	2.1
0.50[b]	-6557	-6717	-11559	2146	1215	0.0049	0.0024	2.0
0.45	-9877	-12757	-16643	14	1208	0.0049	0.0024	2.0

a) χ^2 weights so that the best fit has χ^2= DOF

b) Best fit

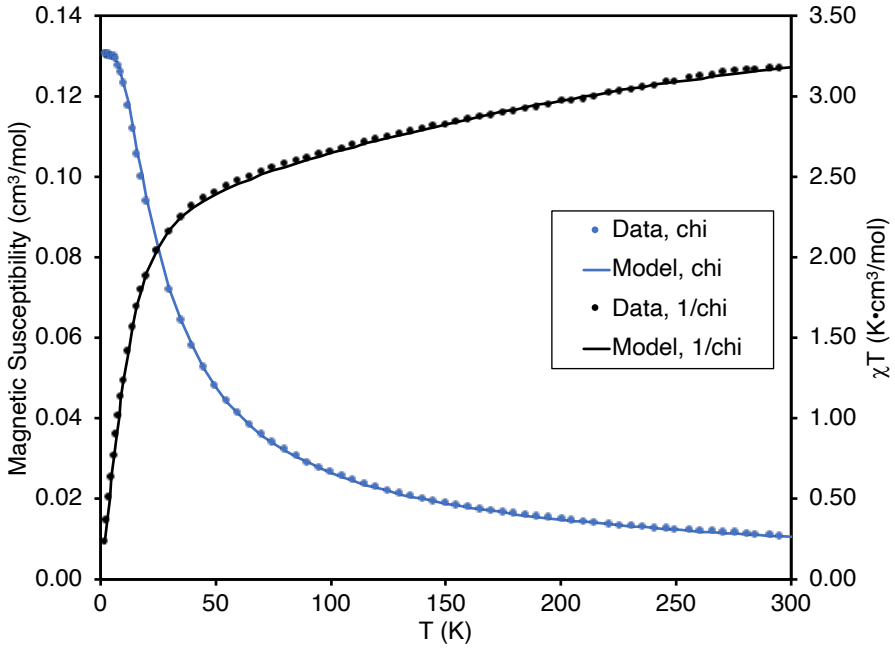

Figure S1. Magnetic susceptibility of Cp'_3Eu and susceptibility modeled with CONDON 3, with k=0.95 (Table S2, row 2).

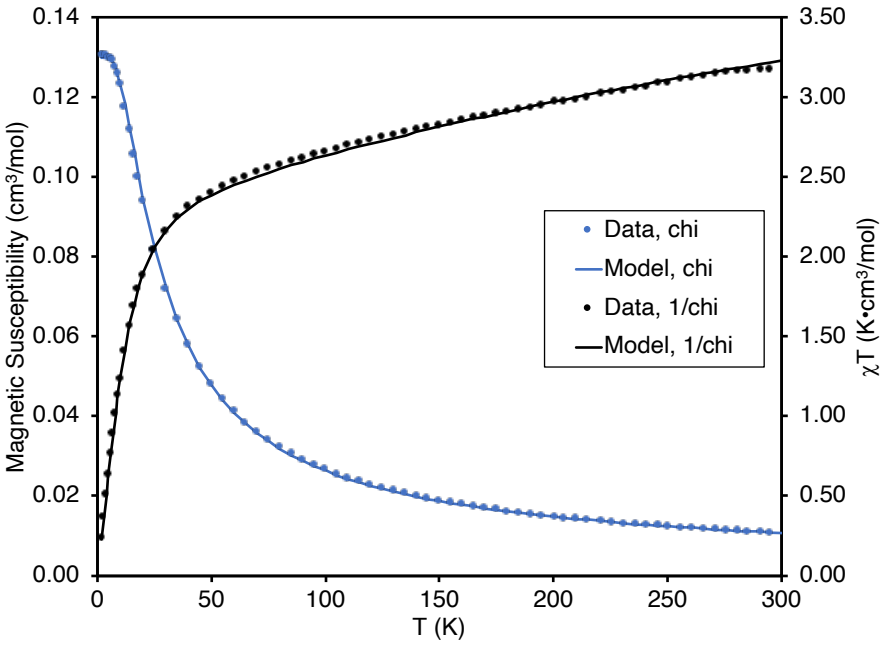

Figure S2. Magnetic susceptibility of Cp'_3Eu and susceptibility modeled with CONDON 3, with k=0.7 (Table S4, row 7).

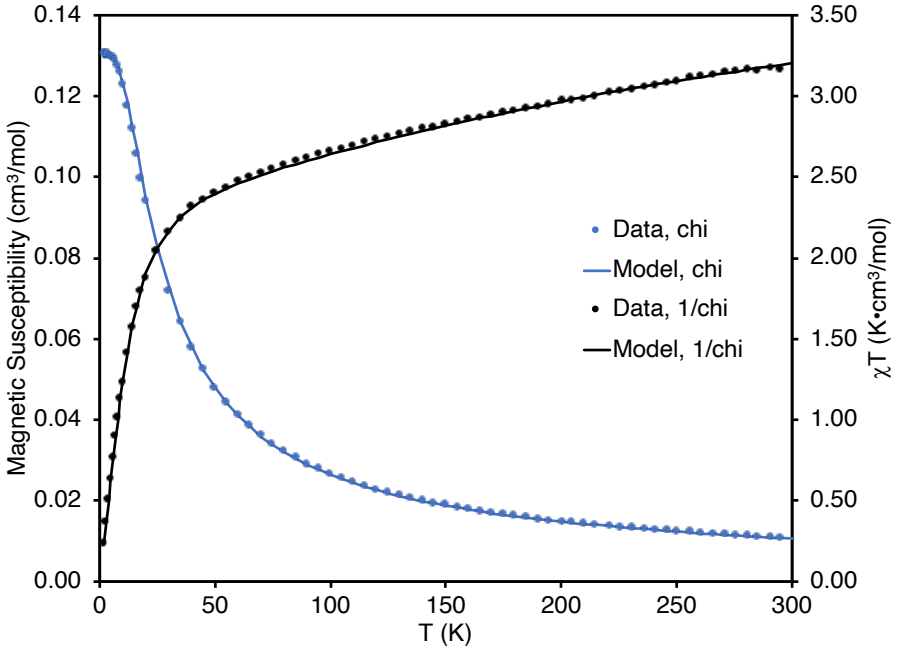

Figure S3. Magnetic susceptibility of Cp'$_3$Eu and susceptibility modeled with CONDON 3, with k=0.55 (Table S4, row 10).

The number of independent data (NID) in the magnetic susceptibility measurement must be known to determine the uncertainty in the value of k and to calculate the reduced chi-squared value (χ_ν^2), which is χ^2 divided by the number of degrees of freedom in the model. The value of NID can be determined using the vanVleck's theorem, which shows that the ground state magnetic susceptibility can be described using two terms, a temperature dependent term (the effective magnetic moment of the state) and a temperature independent term (the temperature independent susceptibility of the state), so the ground state can be described using two pieces of information.[6] Each excited state that is thermally populated over the temperature range contributes three pieces of information – the two previously described plus the energy of the state. In total, the NID is 2 plus 3 times the number of states that become thermally populated. Since Boltzmann statistics show that a state is ~5% populated when the temperature is 1/3 of the energy of the state, we use that to define which states are thermally populated. The value of kT at 298 K is 207 cm^{-1}, so states with energies below 600 cm^{-1} are assumed to be thermally populated. In the case of Cp′$_3$Eu, the CONDON 3 fits show that the ground state is a m_J = 0 singlet state (presumably $|J=0\rangle$), the first excited state is also a singlet at 25 cm^{-1} with m_J = 0 (presumably $|J=1, m_J=0\rangle$) , and the second excited state is a doublet at 533 cm^{-1} with $m_J=\pm1$ ((presumably $|J=1, m_J=\pm1\rangle$). The next exited state is above 900 cm^{-1} and is not thermally populated during the magnetic susceptibility measurement. Since there are 2 excited states with energies less than 600 cm^{-1}, NID is 8 for these measurements.

The parameters being varied are the 4 crystal field parameters (B_0^2, B_0^4, B_0^6, and B_6^6) plus k and sometimes ζ, so the degree of freedom (DOF) of the fits are either 3 or 2 depending whether ζ is allowed to vary. The DOF is used to determine χ_v^2. It is also used to determine the standard deviation of k. Using the fact that the standard deviation of a parameter can be determined by changing its value and leaving it fixed while allowing all of the other parameters in the fit to vary. If χ^2 of the best fit is weighted such that it Is equal to DOF and that weight is applied to the other fits, the standard deviation is the point at which χ^2 increases by 1.[7] For example, in Table S4, the best fit is at k=0.55, so χ^2 for this fit is weighted to 3, the DOF for the fit. χ^2 increases to 4 when k=0.70, so σ(k)=0.15.

C K-Edge and Eu $M_{5,4}$-edge STXM Measurements.

STXM Sample Preparation. 100 nm Si_3N_4 windows used for STXM measurements were purchased from Silson and were baked in an oven at 250 °C overnight before being brought into an Ar-filled glovebox, where they were affixed to an aluminum sample plate. A small amount of each crystalline sample (~1 mg) was dissolved in toluene or hexanes (1 mL), and 1 μL of this solution was transferred to a Si_3N_4 window using a micropipette. The solvent was allowed to evaporate over a few seconds, which deposited thin crystallites of the sample on the Si_3N_4 membrane. The entire sample assembly was then placed under vacuum to remove residue organic solvent. When the sample was fully dried, a second Si_3N_4 window was placed over the sample, sandwiching the crystallites, and the window edges were sealed together using Hardman Double/Bubble epoxy.

Data Acquisition. STXM methodology was similar to that discussed previously.[8-10] Single-energy images and carbon K-edge XAS spectra were acquired using the STXM instrument at the Advanced Light Source-Molecular Environmental Science (ALS-MES) beamline 11.0.2, which is operated in topoff mode at 500 mA, in a ~0.5 atm He-filled chamber.[11] An energy calibration was performed at the C K-edge for CO_2 gas (294.95 eV) and at the Al K-edge for Al metal (1559.0 eV). For these measurements, the X-ray beam was focused with a zone plate onto the sample, and the transmitted light was detected. The spot size and spectral resolution were determined from characteristics of the 25 nm zone plate. Images at a single energy were obtained by raster-scanning the sample and collecting transmitted monochromatic light as a function of sample position. A collection of which is a collection of images were recorded at multiple, closely spaced photon energies across the absorption edge and each collection of images is described as a "stack." Spectra at each image pixel or particular regions of interest on the sample image were extracted from the stack. This enabled spatial mapping of local chemical bonding information. Dwell times used to acquire an image at a single photon energy were ~1 ms per pixel. To quantify the absorbance signal, the measured transmitted intensity (I) was converted to optical density using Beer–Lambert's law: $OD = \ln(I/I0) = \mu\rho d$, where I_0 is the incident photon flux intensity, d is the sample thickness, and μ and ρ are the mass absorption coefficient and density of the sample material, respectively. Incident beam intensity was measured through the sample-free region of the Si_3N_4 windows. Spectra were then obtained by averaging over the crystallites deposited on the substrate. Regions of particles with an absorption of >1.5 OD were omitted to ensure the spectra were in the linear regime of the Beer–Lambert law. The energy resolution was determined to be 0.04 eV and 0.2 eV at the Eu M-edge, and spectra were collected using circularly polarized radiation. During the STXM experiment, samples showed no sign of radiation damage, and each spectrum

was reproduced from multiple independent crystallites. Salient features of the spectra were reproducible using samples prepared from nonoriented polycrystalline particles.

STXM Data Processing. Normalization of the C K-edge data was completed based on a previously described procedure.[12] For each scan, the pre-edge region was fit to a Victoreen polynomial, and that polynomial was extrapolated across the energy range measured. This extrapolated polynomial curve is then subtracted from the experimental data. To normalize the spectral intensity, a line is fit to the post-edge region in this background-subtracted spectrum. Then, this spectrum is divided by a constant so that the intensity at the post-edge normalization energy (302 eV) in the linear fit is equal to one. Once this normalization process is complete for each scan, the normalized spectra are averaged to produce the final, normalized spectrum.

Fits to the C K-edges were performed using the program IGOR Pro 8 and a modified version of EDG_FIT.[13] Pre-edge and rising edge features were modeled by Gaussian line shapes and a step function with a 1:1 ratio of arctangent and error function contributions to represent the rising edge. Fits were performed over several energy ranges with different numbers of curves. The quality of each curve fit was determined by evaluating changes in the χ^2 and by inspecting the residual intensity, which is obtained by subtracting the fit from the experiment and should resemble a horizontal line at zero. The area under the pre-edge peaks (defined as the intensity) was calculated with the formula fwhm × ph × $(1/2)(\pi / \ln 2)^{1/2}$, where fwhm = full width at half maximum height (eV), ph = peak height (normalized intensity), and the value $(1/2)(\pi / \ln 2)^{1/2} \approx 1.065$ is a constant associated with the Gaussian function. Second-derivative spectra of all XAS spectra were used as guides to determine the number and position of peaks, and the smallest possible number of functions was used. For Cp'_3Eu, Cp'_3Gd, and Cp'_3Yb, four Gaussian functions and one step were required to fit the region above 285 eV. Cp'_3Eu and Cp'_3Yb, an additional Gaussian function was required to fit lower energy peaks at 283.6 eV and 284.4 eV, respectively. To obtain a realistic model of the C K-edge data for Cp'_3Gd, the amplitude of the fourth Gaussian function used to model the C 1s → e′ feature was constrained to a value of 0.7.

The Eu $M_{5,4}$-edge data were analyzed in IGOR Pro 8 by first fitting a line to the pre-edge region below 1118 eV which was subsequently subtracted from the experimental data to eliminate the background of the spectra. The data were then normalized by fitting a line to the post-edge region of the spectrum above 1164 eV and setting the edge jump to an intensity of 1.0.

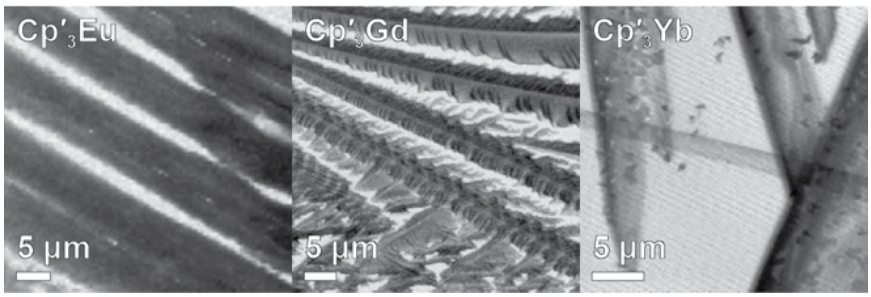

Figure S4. STXM images of Cp'_3Ln crystals used to obtain C K-edge XAS data.

Table S6. Experimental C K-edge peak energies (eV) and intensities (Int)[a] for Cp'_3Ln (Ln = Eu, Yb, and Gd) determined from the curve fits.

Transition Assignment	Energy (eV)	Intensity (Int)[a]
	Cp'_3Eu	
C 1s → a′ ($4f_\pi$*)	283.6	0.08(1)
C 1s → a′ ($5d_\sigma$*)	285.1	0.54(5)
C 1s → e″ ($5d_{\pi+\delta}$*) + e′ ($5d_{\sigma+\pi}$*)	285.8	1.0(1)
	Cp'_3Gd	
C 1s → a′ ($5d_\sigma$*)	285.0	0.16(2)
C 1s → e″ ($5d_{\pi+\delta}$*) + e′ ($5d_{\sigma+\pi}$*)	285.6	1.0(1)
	Cp'_3Yb	
C 1s → a′ ($4f_\pi$*)	284.4	0.07[b]
C 1s → a′ ($5d_\sigma$*)	285.1	0.32(3)
C 1s → e″ ($5d_{\pi+\delta}$*) + e′ ($5d_{\sigma+\pi}$*)	285.6	0.72(7)

[a] Experimental intensities were derived from the area under Gaussian functions used to generate the curve fit and have an estimated error of 10%. [b] The intensity of this feature could not be determined reliably.

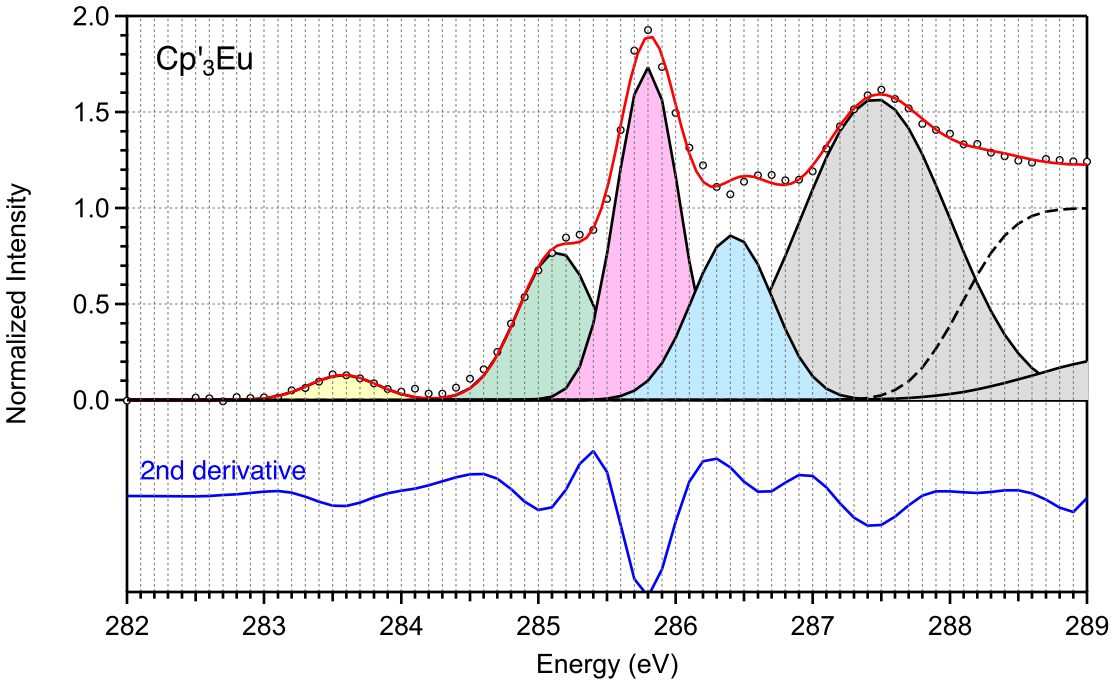

Figure S5. A plot of normalized intensity vs. energy for the C K-edge spectrum of Cp′$_3$Eu collected using STXM. The experimental data (black circles) is shown with the total curve fit (red), and individual Gaussian and step functions which sum to generate the curve fit (yellow, green, pink, blue, and gray). A plot of the 2nd derivative of the experimental data (blue) is provided in the lower panel.

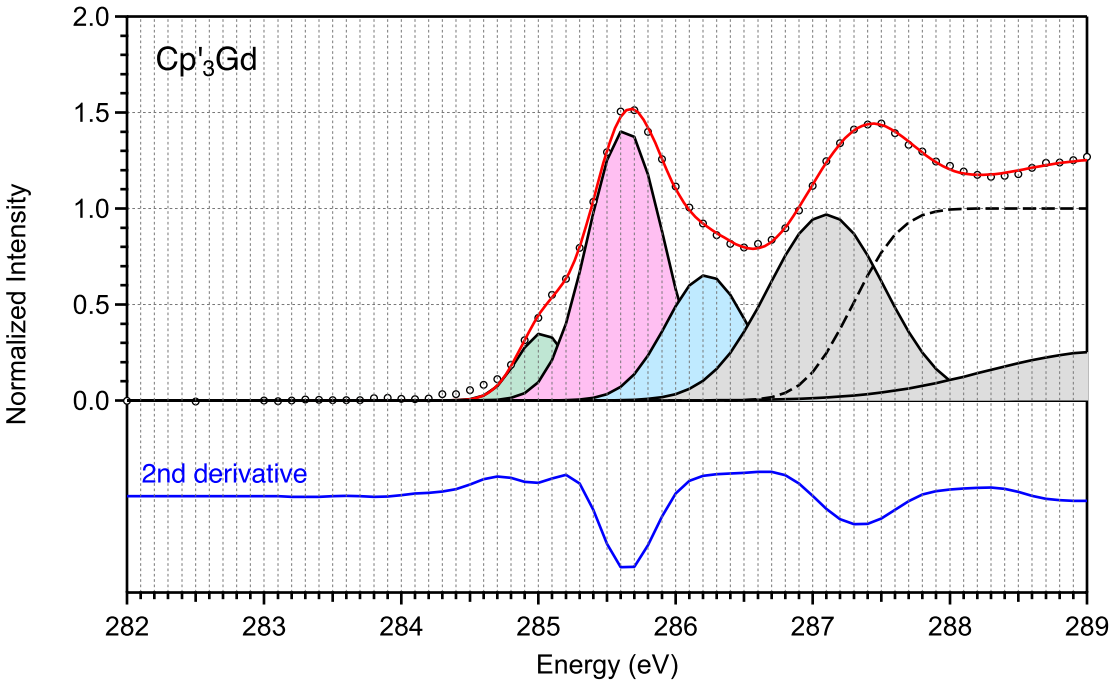

Figure S6. A plot of normalized intensity vs. energy for the C K-edge spectrum of Cp′$_3$Gd collected using STXM. The experimental data (black circles) is shown with the total curve fit (red), and individual Gaussian and step functions which sum to generate the curve fit (yellow, green, pink, blue, and gray). A plot of the 2nd derivative of the experimental data (blue) is provided in the lower panel.

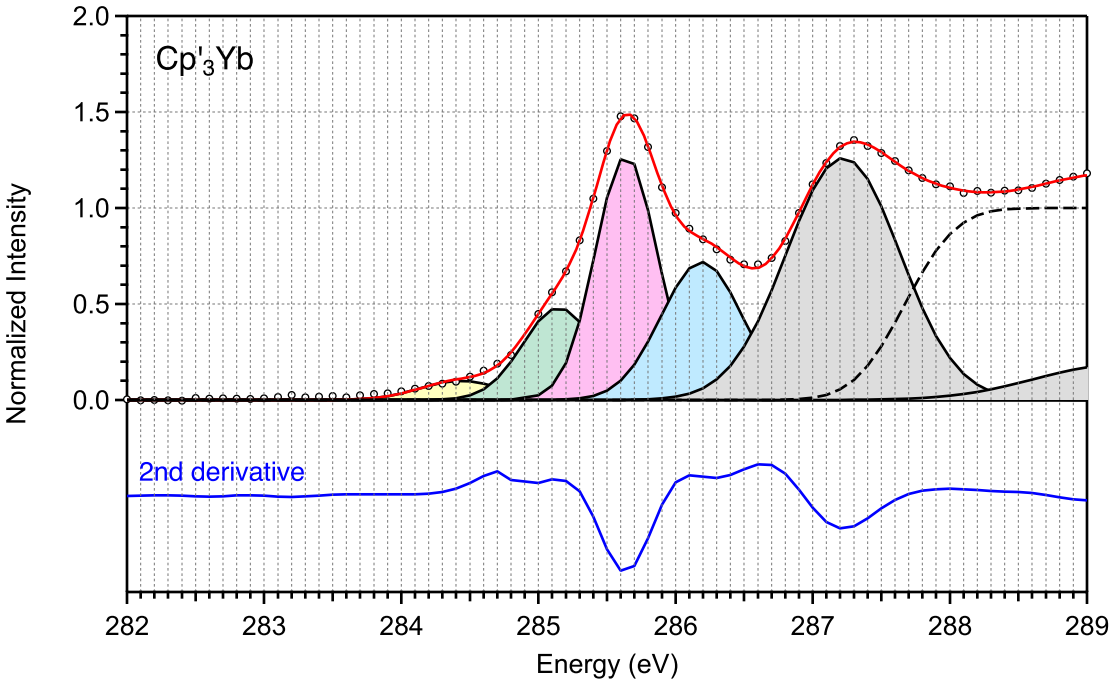

Figure S7. A plot of normalized intensity vs. energy for the C K-edge spectrum of Cp'_3Yb collected using STXM. The experimental data (black circles) is shown with the total curve fit (red), and individual Gaussian and step functions which sum to generate the curve fit (yellow, green, pink, blue, and gray). A plot of the 2nd derivative of the experimental data (blue) is provided in the lower panel.

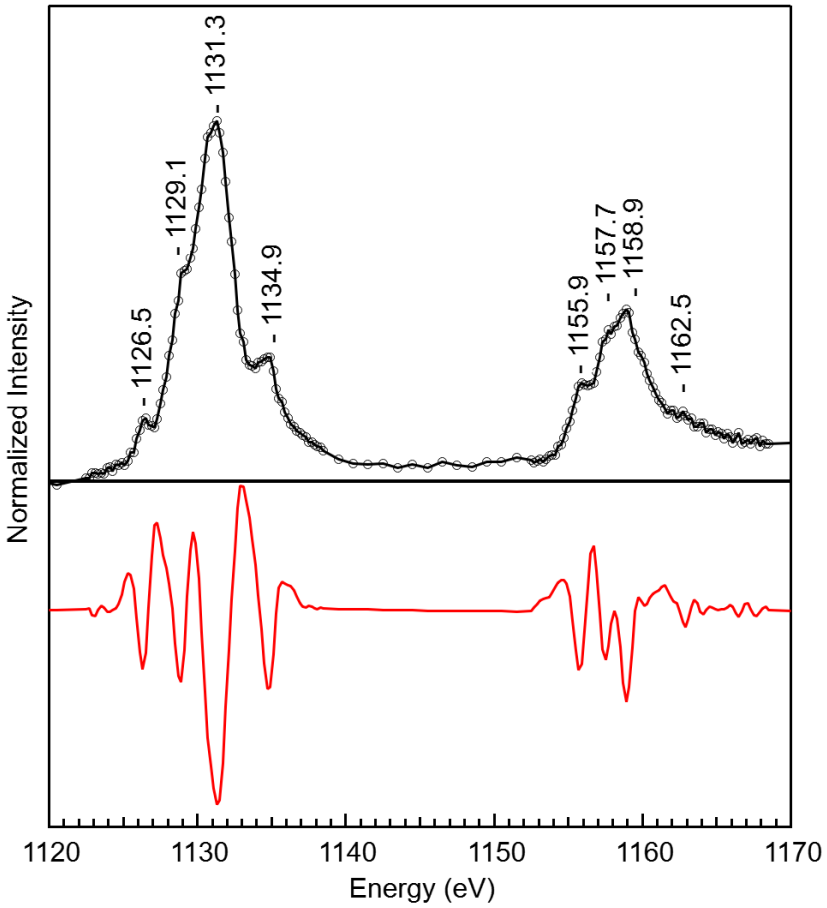

Figure S8. Experimental Eu $M_{5,4}$-edge XAS of Cp'_3Eu (black circles) with 2nd derivative of the data (red). Energies of the Eu $M_{5,4}$-edge XAS features are provided and were determined using the minimum of the 2nd derivative.

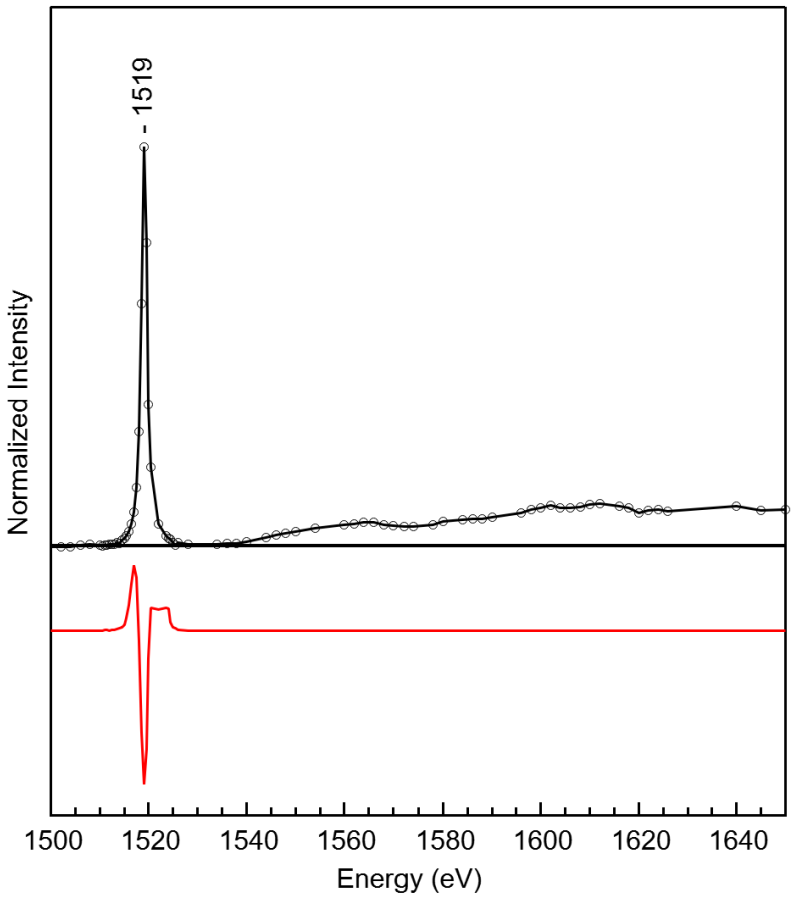

Figure S9. Experimental Yb $M_{5,4}$-edge XAS of Cp'_3Yb (black circles) with 2nd derivative of the data (red). Energies of the Yb $M_{5,4}$-edge XAS features are provided and were determined using the minimum of the 2nd derivative.

Ln L_3 Edge X-ray Absorption Spectroscopy

Data Acquisition. To prepare for data collection, powder samples were ground with a mortar and pestle, diluted with dry boron nitride and packed into the slots of an aluminum holder sealed with indium within an argon dry box. Sample dilution was optimized to achieve absorption step heights less than 1 to avoid thickness effect issues with the lineshape. Since the samples are air sensitive, they were kept under argon until measurement, and the sealed holder was exposed to air for less than one minute during transfer to vacuum. XANES data at the Eu and Yb L_3 absorption edges were collected at Beamline 11-2 of the Stanford Synchrotron Radiation Lightsource using a Si 220 ($\varphi = 0$) monochromator detuned to 50%. The vertical slit height was chosen so that the resolution of the data is core-hole lifetime limited. Data were collected in transmission and energy was calibrated by setting the first inflection point in the absorption spectrum of a Eu_2O_3 standard equal to 6980 eV, as previously reported,[25] and the first inflection point of Yb_2O_3 equal to 8943 eV**.** Data were processed by subtracting a linear pre-edge background and normalizing to unity. Eu L_3-edge data were measured at 50 K and 300 K and the Yb L_3-edge data were collected at 20 K, 100 K, and 300 K, using a liquid He-cooled cryostat to test the effect of temperature on the resulting spectra. An easily-oxidizable sample, $(C_5Me_4H)_3Ce$, was measured along with the samples to ensure that no O_2 had leaked into the sample holder during measurement.

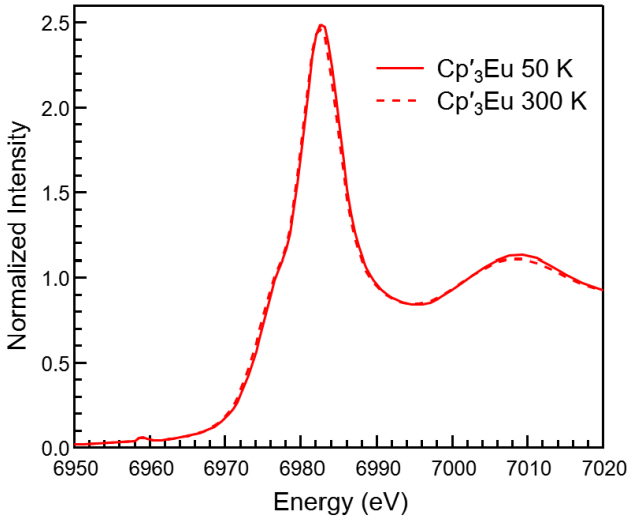

Figure S10. XANES plots of Cp'_3Eu at 50 K and 300 K. XANES spectra do not exhibit differences upon varying temperature.

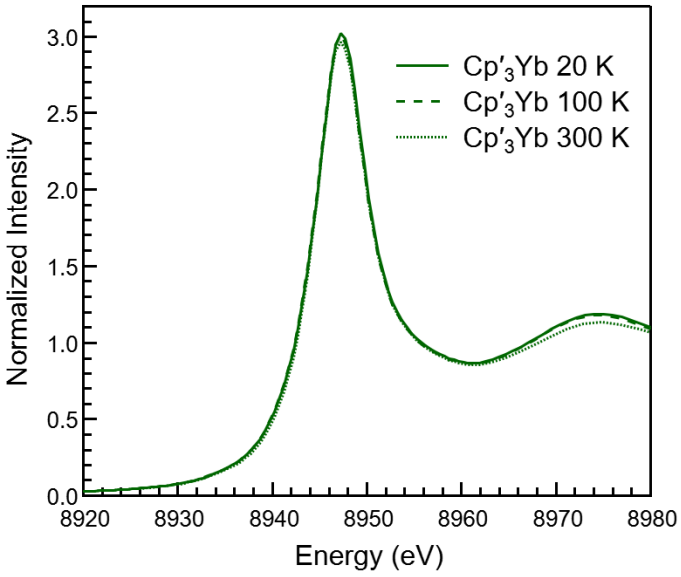

Figure S11. XANES plots of Cp′$_3$Yb at 20, 100, and 300 K. XANES spectra do not exhibit differences upon varying temperature.

Data Processing. XANES data were fit according to previously described methodology[26–28] in order to determine the fraction of 2^+ vs. 3^+ within the samples. The fits consist of a sum of a step-like function to model the absorption edge step and pseudo-Voigts to model the peaks associated with the 2^+ and 3^+ contributions. In addition, a Gaussian is used as a rough model of the first (negative) EXAFS peak in order to account for its effect on the 3+ peak. The edge step is defined as an integrated Lorentzian (arctan) with width Γ equal to the given absorption edge's core-hole lifetime (3.7 eV for Eu L_3 edge and 4.2 eV for Yb L_3 edge).[14] The pseudo-Voigts are defined with half Lorentzian and half Gaussian character and use the same value of Γ as the edge step, with the Gaussian width, σ, (held equal for the 2+ and 3+ components) allowed to vary.. The edge position, E_0, is constrained to the average of the peak energies of 2^+ and 3^+ weighted by their peak areas in order to reduce the number of parameters in the fit and to control correlations between the fit parameters. Results from the fit are shown in Fig. S13 – S14 with parameters shown in Tables S7 to S10. We note that in each case, the presence of the divalent peak is confirmed with an F-test with >99% confidence.

Table S7. Edge and peak energies from fits to Cp'$_3$Eu and Cp'$_3$Yb XANES data. Error bars for individual parameters were calculated using the covariance matrix assuming normal distributions for variances in the data and a data resolution set by the core-hole lifetime. Parameters reported without error bars were held fixed during the fit or constrained as described in the text.

Sample	E_0 **(eV)**	E_{2+} **(eV)**	E_{3+} **(eV)**	E_{EXAFS} **(eV)**
Cp′$_3$Eu	6980.8	6976.5 ± 0.4	6982.5 ± 0.2	6996.0
Cp′$_3$Yb	8945.3	8939.9 ± 0.8	8946.0 ± 0.1	8960.6

Table S8. Gaussian peak widths from fits to Cp'$_3$Eu and Cp'$_3$Yb XANES data. The 2+ and 3+ peaks are pseudo-Voigts with Lorentzian parameters described in the text. The EXAFS peak is a pure Gaussian.

Sample	σ_{2+} **(eV)**	σ_{3+} **(eV)**	σ_{EXAFS} **(eV)**
Cp′$_3$Eu	3.1	3.1 ± 0.4	4.4 ± 2.7
Cp′$_3$Yb	3.0	3.0 ± 0.2	3.4 ± 1.3

Table S9. 2+ fractions calculated from XANES fitting. Areas under the 2+ and 3+ peaks as determined from XANES fitting using Gaussians are shown. These areas were in turn used to calculate the 2+ fraction within the sample.

Sample	**2$^+$ peak area**	**3$^+$ peak area**	**EXAFS peak area**	**fraction 2$^+$**
Cp′$_3$Eu	5.2 ± 0.8	13.0 ± 1.0	-1.8± 0.9	0.28 ± 0.04
Cp′$_3$Yb	2.8 ± 0.8	21.6 ± 1.0	-1.8± 0.9	0.11 ± 0.03

Table S10. R(%) values (goodness of fit) for the XANES fits.

Sample	**R(%) from Fit**
Cp′$_3$Eu	5.2
Cp′$_3$Yb	4.3

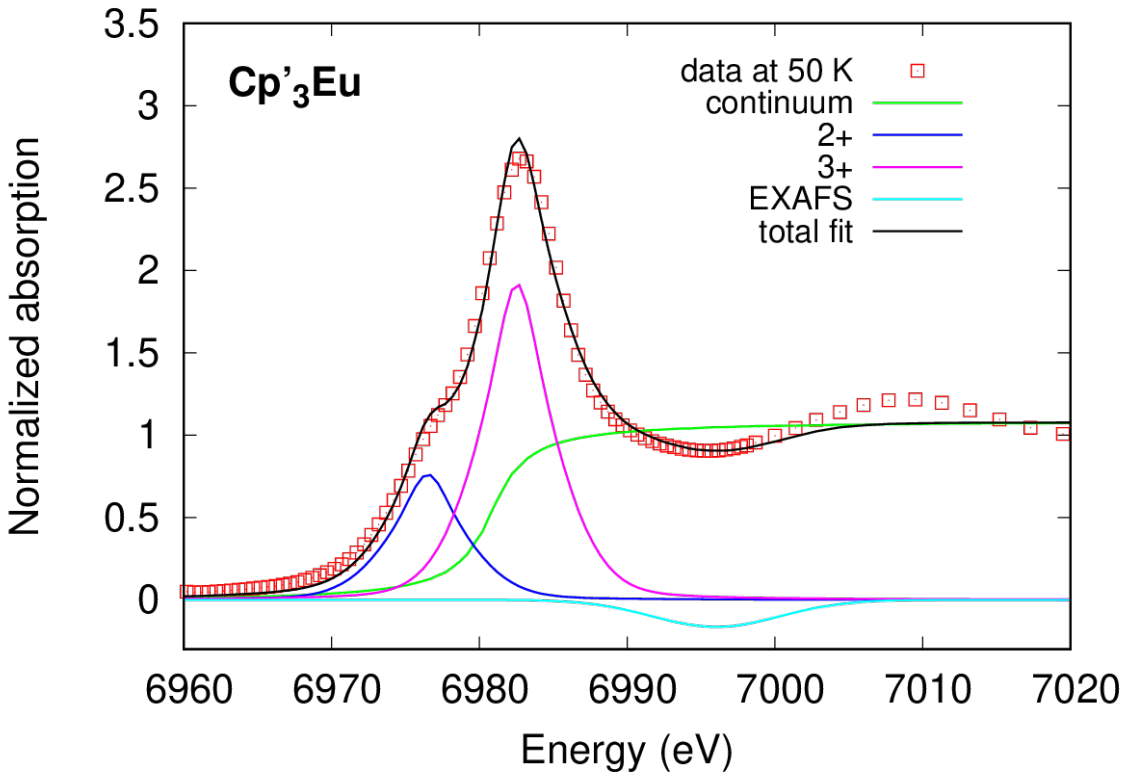

Figure S12. Normalized XANES data at 50 K, fit, and fit components for Cp′$_3$Eu.

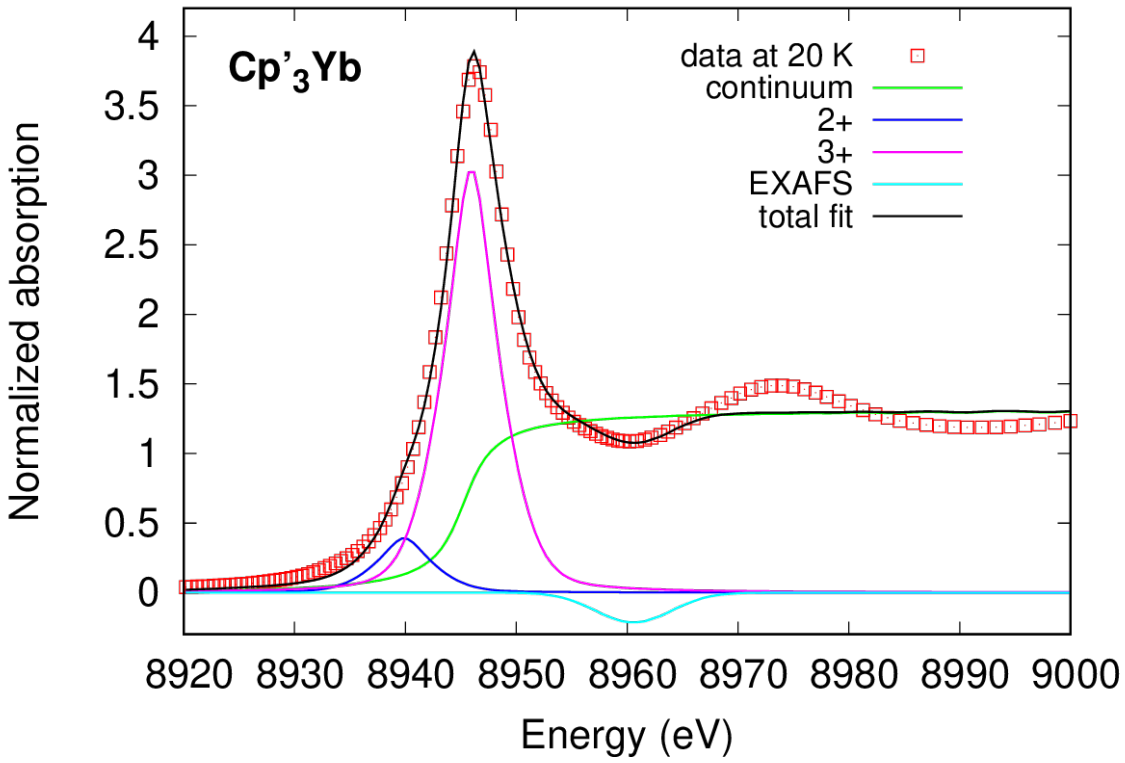

Figure S13. Normalized XANES data at 20 K, fit, and fit components for Cp′$_3$Yb.

Computational Details. All calculations were performed using unrestricted density functional theory (DFT) with the NWChem computational chemistry software.[15] Small core Stuttgart relativistic ECPs (replacing 28 electrons) and corresponding basis sets[16] were used for the lanthanides, whereas the DFT optimized TZVP basis sets[17] were used for the other elements in the molecular complexes (C, H, Si). The long-range corrected LC-PBE0 functional was used,[18] which has shown to produce accurate spectra.[19] The molecular structures of the complexes were optimized for both functionals, starting from the experimentally determined structure. Coordinates of the optimized structures can be found in Table S7 XAS spectra were calculated using linear response time-dependent DFT (TDDFT) implementation in NWChem. The configuration interaction singles (CIS) approximation[20] combined with the restricted energy window approach[21] was used to calculate the first 500 excited states representing single excitations from the relevant carbon core-orbitals. The calculated excitation energies and intensities were uniformly Gaussian broadened to generate the spectra. A broadening of 0.5 eV at full-width half-maximum was found to produce peak widths that agree well with those obtained in the experiments. The calculated XAS excitation energies are lower than those in the experiment. To properly align the calculated and experimental spectra, the calculated excited states were shifted by 9.4 eV.

Table S11. Optimized geometry for Eu complex with the LC-PBE0 functional.

Eu	0.64134205	6.01011171	3.42828209
Si	1.84233835	8.71071786	0.89573254
Si	-1.98693091	9.16458338	4.31083454
Si	2.05994552	2.72428715	5.18674468
C	0.75916602	5.99125647	0.73634419
C	1.10239171	4.68748220	1.12298064
C	2.33783653	4.74787373	1.77208733
C	2.74960632	6.08944239	1.78843942
C	1.77515597	6.87570786	1.14511296
C	3.44536991	9.19270644	0.08138932
C	0.40249983	9.23772533	-0.16038944
C	1.75867553	9.51748387	2.58275472
C	-1.73977627	6.27989735	4.68429336
C	-1.83206587	5.10971953	3.92084022
C	-1.83012749	5.47983655	2.57233800
C	-1.73646739	6.87941833	2.51369313
C	-1.68160653	7.39591097	3.82237443
C	-3.70343209	9.26250206	5.03182137
C	-0.78715075	9.77350899	5.60569569
C	-1.91091676	10.24590233	2.79398979
C	2.86729549	5.52077873	4.86851058
C	2.45347006	6.80098683	5.25541080
C	1.24603426	6.66633773	5.94955065
C	0.92576663	5.30035789	5.98899770
C	1.92170473	4.57255474	5.31276315
C	3.80374249	2.29123208	4.69171120
C	1.66832959	1.97922250	6.84890855

C	0.85835649	2.03258592	3.93249568
H	-0.13609495	6.27049267	0.19589887
H	0.52369225	3.79308917	0.92790786
H	2.88928636	3.90795265	2.17449672
H	3.67844947	6.45569395	2.20807158
H	3.52242336	8.74837163	-0.91388963
H	4.30197693	8.84633053	0.66538123
H	3.52749806	10.27796980	-0.02285232
H	0.44698277	8.75200106	-1.13869241
H	0.41113611	10.31866224	-0.32412398
H	-0.55548496	8.98306620	0.29953062
H	0.88504017	9.17690125	3.15063642
H	1.69300020	10.60749585	2.52117056
H	2.65252667	9.27291277	3.16375575
H	-1.74789001	6.32410549	5.76603124
H	-1.91040277	4.10129328	4.30778580
H	-1.90116182	4.81046263	1.72515661
H	-1.74687401	7.47180955	1.60710294
H	-3.95060580	10.28422081	5.33330992
H	-3.79548971	8.61993205	5.91128114
H	-4.44774729	8.93229487	4.30308391
H	-1.00406641	10.81714167	5.85124466
H	0.25496801	9.71856031	5.28168880
H	-0.88698296	9.19790938	6.53017153
H	-2.16596232	11.27656899	3.05584690
H	-2.63299856	9.91094223	2.04424889
H	-0.92244713	10.25801602	2.32989591
H	3.78014263	5.28729669	4.33607303
H	2.98615212	7.72630263	5.07539432
H	0.67462135	7.46977563	6.39513494
H	0.06045648	4.87349492	6.48060976
H	4.51762688	2.66491178	5.43019954
H	4.07697091	2.71481835	3.72183303
H	3.92884630	1.20733284	4.62294008
H	0.65224073	2.23036781	7.16455456
H	2.35396436	2.35369133	7.61273160
H	1.74824530	0.88909619	6.82303824
H	-0.17307503	2.28508751	4.19473380
H	0.92726607	0.94196418	3.88981449
H	1.05314980	2.41634617	2.92746080

References

1. M. R. MacDonald, J. E. Bates, J. W. Ziller, F. Furche and W. J. Evans, *J. Am. Chem. Soc.*, 2013, **135**, 9857-9868.
2. M. E. Fieser, M. R. MacDonald, B. T. Krull, J. E. Bates, J. W. Ziller, F. Furche and W. J. Evans, *J. Am. Chem. Soc.*, 2015, **137**, 369-382.
3. M. Speldrich, J. van Leusen and P. Kögerler, *J. Comput. Chem.*, 2018, **39**, 2133-2145.
4. S. Jank, H. Reddmann, H.-D. Amberger and C. Apostolidis, *J. Organomet. Chem.*, 2004, **689**, 3143-3157.
5. R. M. Hammond, M. F. Reid and F. S. Richardson, *J. Less-Common Met.*, 1989, **148**, 311-319.

6. J. H. Van Vleck, *The Theory of Electric and Magnetic Susceptibilities*, Oxford University Press, 1932.
7. W. H. Press, B. P. Flannery and S. A. Teukolsky, *Numerical Recipes in Fortran 77: The Art of Scientific Computing 2nd Edition*, Cambridge University Press, 1992.
8. S. G. Minasian, J. M. Keith, E. R. Batista, K. S. Boland, S. A. Kozimor, R. L. Martin, D. K. Shuh, T. Tyliszczak and L. J. Vernon, *J. Am. Chem. Soc.*, 2013, **135**, 14731-14740.
9. S. G. Minasian, J. M. Keith, E. R. Batista, K. S. Boland, D. L. Clark, S. A. Kozimor, R. L. Martin, D. K. Shuh and T. Tyliszczak, *Chem. Sci.*, 2014, **5**, 351-359.
10. M. W. Löble, J. M. Keith, A. B. Altman, S. C. E. Stieber, E. R. Batista, K. S. Boland, S. D. Conradson, D. L. Clark, J. Lezama Pacheco, S. A. Kozimor, R. L. Martin, S. G. Minasian, A. C. Olson, B. L. Scott, D. K. Shuh, T. Tyliszczak, M. P. Wilkerson and R. A. Zehnder, *J. Am. Chem. Soc.*, 2015, **137**, 2506-2523.
11. H. Bluhm, K. Andersson, T. Araki, K. Benzerara, G. E. Brown, J. J. Dynes, S. Ghosal, M. K. Gilles, H. C. Hansen, J. C. Hemminger, A. P. Hitchcock, G. Ketteler, A. L. D. Kilcoyne, E. Kneedler, J. R. Lawrence, G. G. Leppard, J. Majzlan, B. S. Mun, S. C. B. Myneni, A. Nilsson, H. Ogasawara, D. F. Ogletree, K. Pecher, M. Salmeron, D. K. Shuh, B. Tonner, T. Tyliszczak, T. Warwick and T. H. Yoon, *J. Electron. Spectrosc. Relat. Phenom.*, 2006, **150**, 86-104.
12. D. E. Smiles, E. R. Batista, C. H. Booth, D. L. Clark, J. M. Keith, S. A. Kozimor, R. L. Martin, S. G. Minasian, D. K. Shuh, S. C. E. Stieber and T. Tyliszczak, *Chem. Sci.*, 2020, **11**, 2796-2809.
13. G. N. George, *Journal*.
14. O. Keski-Rahkonen and M. O. Krause, *At. Data Nucl. Data Tables*, 1974, **14**, 139-146.
15. E. Aprà, E. J. Bylaska, W. A. de Jong, N. Govind, K. Kowalski, T. P. Straatsma, M. Valiev, H. J. J. van Dam, Y. Alexeev, J. Anchell, V. Anisimov, F. W. Aquino, R. Atta-Fynn, J. Autschbach, N. P. Bauman, J. C. Becca, D. E. Bernholdt, K. Bhaskaran-Nair, S. Bogatko, P. Borowski, J. Boschen, J. Brabec, A. Bruner, E. Cauët, Y. Chen, G. N. Chuev, C. J. Cramer, J. Daily, M. J. O. Deegan, T. H. Dunning, Jr., M. Dupuis, K. G. Dyall, G. I. Fann, S. A. Fischer, A. Fonari, H. Früchtl, L. Gagliardi, J. Garza, N. Gawande, S. Ghosh, K. Glaesemann, A. W. Götz, J. Hammond, V. Helms, E. D. Hermes, K. Hirao, S. Hirata, M. Jacquelin, L. Jensen, B. G. Johnson, H. Jónsson, R. A. Kendall, M. Klemm, R. Kobayashi, V. Konkov, S. Krishnamoorthy, M. Krishnan, Z. Lin, R. D. Lins, R. J. Littlefield, A. J. Logsdail, K. Lopata, W. Ma, A. V. Marenich, J. Martin del Campo, D. Mejia-Rodriguez, J. E. Moore, J. M. Mullin, T. Nakajima, D. R. Nascimento, J. A. Nichols, P. J. Nichols, J. Nieplocha, A. Otero-de-la-Roza, B. Palmer, A. Panyala, T. Pirojsirikul, B. Peng, R. Peverati, J. Pittner, L. Pollack, R. M. Richard, P. Sadayappan, G. C. Schatz, W. A. Shelton, D. W. Silverstein, D. M. A. Smith, T. A. Soares, D. Song, M. Swart, H. L. Taylor, G. S. Thomas, V. Tipparaju, D. G. Truhlar, K. Tsemekhman, T. Van Voorhis, Á. Vázquez-Mayagoitia, P. Verma, O. Villa, A. Vishnu, K. D. Vogiatzis, D. Wang, J. H. Weare, M. J. Williamson, T. L. Windus, K. Woliński, A. T. Wong, Q. Wu, C. Yang, Q. Yu, M. Zacharias, Z. Zhang, Y. Zhao and R. J. Harrison, *J. Chem. Phys.*, 2020, **152**, 184102.
16. M. Dolg, H. Stoll and H. Preuss, *J. Chem. Phys.*, 1989, **90**, 1730-1734.
17. N. Godbout, D. R. Salahub, J. Andzelm and E. Wimmer, *Can. J. Chem.*, 1992, **70**, 560-571.
18. M. A. Rohrdanz and J. M. Herbert, *J. Chem. Phys.*, 2008, **129**, 034107.

19. M. Srebro, N. Govind, W. A. de Jong and J. Autschbach, *The Journal of Physical Chemistry A*, 2011, **115**, 10930-10949.
20. J. B. Foresman, M. Head-Gordon, J. A. Pople and M. J. Frisch, *The Journal of Physical Chemistry*, 1992, **96**, 135-149.
21. K. Lopata, B. E. Van Kuiken, M. Khalil and N. Govind, *Journal of Chemical Theory and Computation*, 2012, **8**, 3284-3292.